

# Evaluation of measurement accuracy of $h \rightarrow \tau^+\tau^-$ branching ratio at the ILC with $\sqrt{s} = 250$ GeV and 500 GeV

Shin-ichi Kawada<sup>1,†</sup>, Keisuke Fujii<sup>2</sup>, Taikan Suehara<sup>3</sup>,  
Tohru Takahashi<sup>1</sup>, Tomohiko Tanabe<sup>4</sup>

June 24, 2018

- 1: Advanced Sciences of Matter (AdSM), Hiroshima University, 1-3-1, Kagamiyama, Higashi-Hiroshima, Hiroshima, 739-8530, Japan  
 2: High Energy Accelerator Research Organization (KEK), 1-1, Oho, Tsukuba, Ibaraki, 305-0801, Japan  
 3: Department of Physics, Tohoku University, 6-3, Aoba, Aramaki, Aoba-ku, Sendai, Miyagi, 980-8578, Japan  
 4: International Center for Elementary Particle Physics (ICEPP), The University of Tokyo, 7-3-1, Hongo, Bunkyo-ku, Tokyo, 113-0033, Japan

† : s-kawada@huhep.org

## Abstract

<sup>1</sup> We evaluate the measurement accuracy of the branching ratio of  $h \rightarrow \tau^+\tau^-$  at  $\sqrt{s} = 250$  GeV and 500 GeV at the ILC with the ILD detector simulation. For the  $\sqrt{s} = 250$  GeV, we assume the Higgs mass of  $M_h = 120$  GeV, branching ratio of  $\text{Br}(h \rightarrow \tau^+\tau^-) = 8.0$  %, beam polarization of  $P(e^-, e^+) = (-0.8, +0.3)$ , and integrated luminosity of  $\int L dt = 250 \text{ fb}^{-1}$ . The Higgs-strahlung process  $e^+e^- \rightarrow Zh$  with  $Z \rightarrow e^+e^-$ ,  $Z \rightarrow \mu^+\mu^-$ ,  $Z \rightarrow q\bar{q}$  mode are analyzed. The measurement accuracy is calculated to be  $\Delta(\sigma \cdot \text{Br})/(\sigma \cdot \text{Br}) = 3.5$  %. The scaled result to  $M_h = 125$  GeV is estimated to be 4.2 %. For the  $\sqrt{s} = 500$  GeV, we assume the Higgs mass of  $M_h = 125$  GeV, branching ratio of  $\text{Br}(h \rightarrow \tau^+\tau^-) = 6.32$  %, beam polarization of  $P(e^-, e^+) = (-0.8, +0.3)$ , and integrated luminosity of  $\int L dt = 500 \text{ fb}^{-1}$ . The Higgs-strahlung process  $e^+e^- \rightarrow Zh$  with  $Z \rightarrow q\bar{q}$  mode and  $WW$ -fusion process  $e^+e^- \rightarrow \nu_e \bar{\nu}_e h$  are analyzed. The measurement accuracy is calculated to be  $\Delta(\sigma \cdot \text{Br})/(\sigma \cdot \text{Br}) = 5.7$  % for Higgs-strahlung with  $Z \rightarrow q\bar{q}$  and 7.5 % for  $WW$ -fusion.

## 1 Introduction

Since the discovery of Higgs boson by the ATLAS and the CMS experiments [1, 2], one of the next important themes for particle physics is the investigation of Higgs boson, especially the mass generation mechanism. One of the important properties of Higgs boson is its branching ratio. In the Standard Model (SM) of particle physics, the Yukawa coupling constant of matter fermions with the Higgs boson is proportional to the fermion mass. However, if there are new physics, the coupling constant will deviate from the SM prediction. Besides, the deviation from the SM can be the few-percent level if no additional new particles are to be found at the LHC [3]. Therefore, measuring the branching ratio precisely is a crucial problem from the viewpoint of new physics.

In this document, we focus on the branching ratio of  $h \rightarrow \tau^+\tau^-$ . We estimate the measurement accuracy  $\Delta(\sigma \cdot \text{Br})/(\sigma \cdot \text{Br})$  of the  $h \rightarrow \tau^+\tau^-$  branching ratio at  $\sqrt{s} = 250$  GeV and 500 GeV at the ILC with the ILD full detector simulation.

## 2 Signal and Background

### 2.1 Signals

There are several Higgs production process as summarized in Figure 1.

The Higgs-strahlung process  $e^+e^- \rightarrow Zh$  is the dominant process at  $\sqrt{s} = 250$  GeV. There are three types of signal depending on the decay of  $Z$  boson, as shown in Figure 2. The most sensitive channel at  $\sqrt{s} = 250$  GeV is  $Z \rightarrow q\bar{q}$  mode because of the high statistics. In this document, we concentrate on  $Z \rightarrow \ell^+\ell^-$  mode and  $Z \rightarrow q\bar{q}$  mode, because  $Z \rightarrow \nu\bar{\nu}$  mode contributes negligibly than  $Z \rightarrow q\bar{q}$  mode. Besides, we only consider  $Z \rightarrow e^+e^-$  mode and  $Z \rightarrow \mu^+\mu^-$  mode as the signal process of the analysis of  $Z \rightarrow \ell^+\ell^-$  mode. The cross section of  $Z \rightarrow q\bar{q}$  mode is 19.8 fb,  $Z \rightarrow \ell^+\ell^-$  mode is 1.9 fb, respectively.

<sup>1</sup>This write-up is intended to supplement a white paper on the Higgs physics at the ILC. A white paper on the Higgs physics at the ILC to be submitted to the Snowmass process 2013.

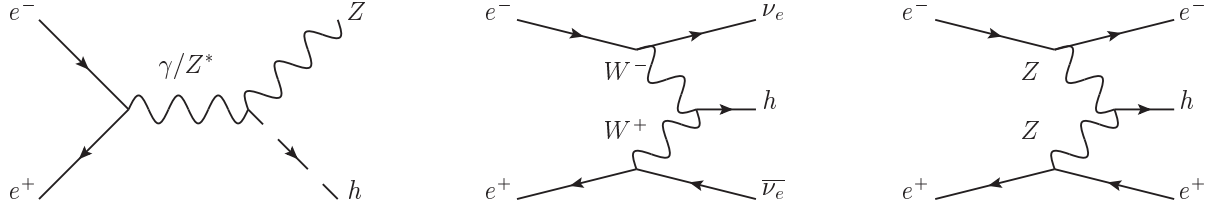


Figure 1: The diagrams of Higgs production processes. (left): Higgs-strahlung process, (middle):  $WW$ -fusion process, (right):  $ZZ$ -fusion process.

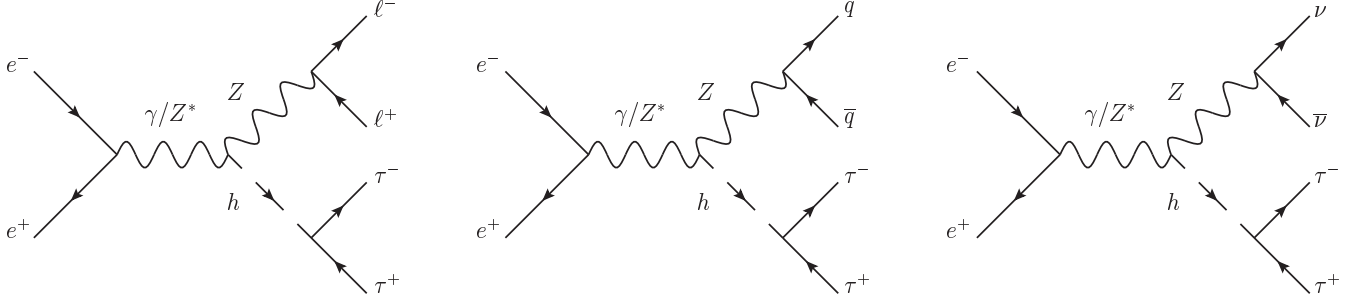


Figure 2: The diagrams of Higgs-strahlung process with  $Z$  boson decay. (left):  $Z \rightarrow \ell^+ \ell^-$  mode, (middle):  $Z \rightarrow q \bar{q}$  mode, (right):  $Z \rightarrow \nu \bar{\nu}$  mode.

At the  $\sqrt{s} = 500$  GeV, the  $WW$ -fusion process and  $Z \rightarrow q \bar{q}$  mode of Higgs-strahlung process contributes significantly. We concentrate on these two modes of the analyses of  $\sqrt{s} = 500$  GeV, and we ignore other processes from the analyses. The cross section of  $WW$ -fusion and Higgs-strahlung at  $\sqrt{s} = 500$  GeV is 149.5 fb and 100.4 fb.

## 2.2 Backgrounds

For the  $Z \rightarrow \ell^+ \ell^-$  mode, the possible backgrounds are the processes which including four leptons in the final state. The left diagram of Figure 3 shows the example of  $\mu^+ \mu^- \tau^+ \tau^-$  process via  $e^+ e^- \rightarrow ZZ$ . Other possible processes are  $e^+ e^- \rightarrow Zh$  reactions with the Higgs boson does not decay to tau pairs ( $H \not\rightarrow \tau^+ \tau^-$ ).

For the  $Z \rightarrow q \bar{q}$  mode, the  $q \bar{q} q \bar{q}$ ,  $q \bar{q} \ell^+ \ell^-$ , and  $q \bar{q} \ell \nu$  which comes from  $e^+ e^- \rightarrow W^+ W^-$  and  $e^+ e^- \rightarrow ZZ$  processes should be the main background. The middle diagram of Figure 3 shows the background of  $e^+ e^- \rightarrow WW \rightarrow q \bar{q} \tau \nu$  process.

On the other hand, the possible backgrounds for  $WW$ -fusion process are  $e^+ e^- \rightarrow W^+ W^- \rightarrow \tau^+ \bar{\nu} \tau^- \nu$  and  $e^+ e^- \rightarrow \nu \nu Z$  with  $Z \rightarrow \tau^+ \tau^-$ . The diagram of latter process is shown in the right of Figure 3.

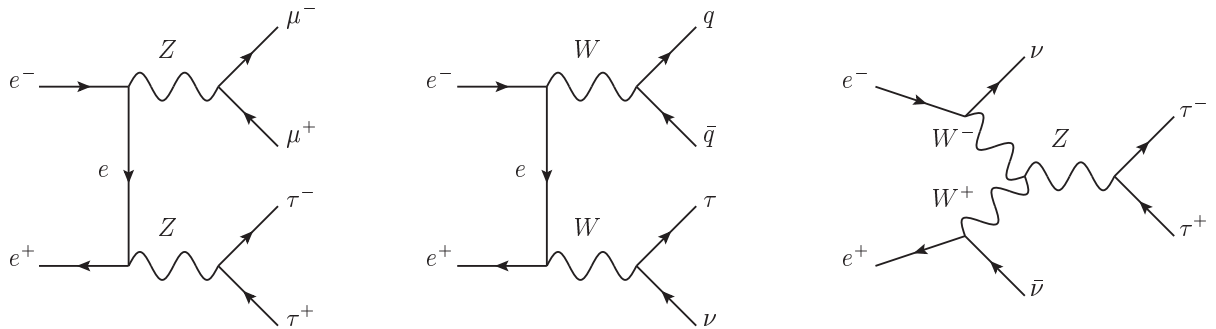


Figure 3: The example diagrams of backgrounds. (left):  $\mu^+ \mu^- \tau^+ \tau^-$  background for  $Z \rightarrow \ell^+ \ell^-$  mode, (middle):  $q \bar{q} \tau \nu$  background for  $Z \rightarrow q \bar{q}$  mode, (right):  $\nu \bar{\nu} \tau^+ \tau^-$  background for  $WW$ -fusion process.

### 3 Simulation Conditions

We perform the detector simulation with **Mokka** [4], a Geant4-based [5] full simulation, with the ILD detector model. **TAUOLA** [6] is used for the tau decay simulation. The ILD detector model consists of a vertex detector, a time projection chamber (TPC), an electromagnetic calorimeter (ECAL), a hadronic calorimeter (HCAL), a return yoke, muon systems, and forward components.

For the analysis of  $\sqrt{s} = 250$  GeV, we use the signal and background samples which were generated in the context of the Letter of Intent [7], and use ILD\_00 detector model. The effects of beamstrahlung and initial state radiation are included. We assume a Higgs mass of  $M_h = 120$  GeV, a branching ratio of  $\text{Br}(h \rightarrow \tau^+\tau^-) = 8.0\%$  as assumed by **PYTHIA** [9], an integrated luminosity of  $\int L dt = 250 \text{ fb}^{-1}$ , and a beam polarization of  $P(e^+, e^-) = (+0.3, -0.8)$ . We also rescale the final result to the case of  $M_h = 125$  GeV and the  $h \rightarrow \tau^+\tau^-$  branching ratio which includes the NNLO corrections [10].

For the analysis of  $\sqrt{s} = 500$  GeV, we use the signal and background samples which were generated in the context of ILC Technical Design Report [11–14], and use ILD\_o1\_v05 model. In these samples, the effects of  $\gamma\gamma \rightarrow \text{hadron(s)}$  overlay process are also included. We use the processes of  $q\bar{q}h$ ,  $\nu\bar{\nu}h$ ,  $\ell^+\ell^-h$ , 2f, 4f, 5f, 6f, and  $\gamma\gamma \rightarrow 4f$  (f = fermions). We assume a Higgs mass of  $M_h = 125$  GeV, a branching ratio of  $\text{Br}(h \rightarrow \tau^+\tau^-) = 6.32\%$  [10], an integrated luminosity of  $\int L dt = 500 \text{ fb}^{-1}$ , and a beam polarization of  $P(e^+, e^-) = (+0.3, -0.8)$ .

### 4 Event Reconstruction and Event Selection

#### 4.1 $Z \rightarrow \ell^+\ell^-$ mode at $\sqrt{s} = 250$ GeV

In this mode, we take the strategy of reconstructing the  $Z$  boson first, followed by the reconstruction of the tau pairs from the Higgs decay.

We apply lepton identification at first for dividing  $Z \rightarrow e^+e^-$  events and  $Z \rightarrow \mu^+\mu^-$  events by using the information of energy deposit in the calorimeter ( $E_{\text{ECAL}}$  and  $E_{\text{HCAL}}$ , where  $E_{\text{ECAL(HCAL)}}$  is the energy deposit in ECAL(HCAL)) and track momentum ( $P_{\text{track}}$ ). Figures 4 - 7 are the plots of  $E_{\text{ECAL}}/(E_{\text{ECAL}} + E_{\text{HCAL}})$  and  $(E_{\text{ECAL}} + E_{\text{HCAL}})/P_{\text{track}}$ .

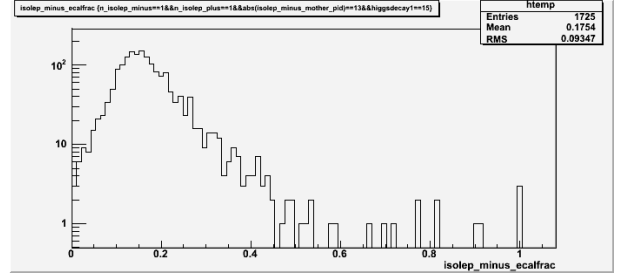
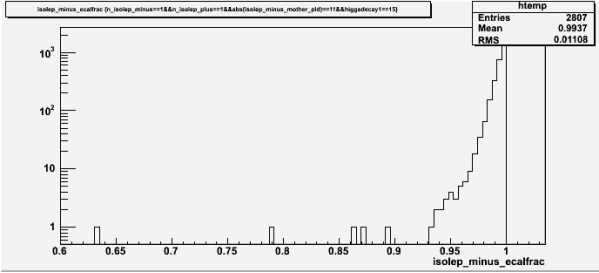


Figure 4: The plot of  $E_{\text{ECAL}}/(E_{\text{ECAL}} + E_{\text{HCAL}})$  for the  $e$  in  $e^+e^-h$  samples.

Figure 5: The plot of  $E_{\text{ECAL}}/(E_{\text{ECAL}} + E_{\text{HCAL}})$  for the  $\mu$  in  $\mu^+\mu^-h$  samples.

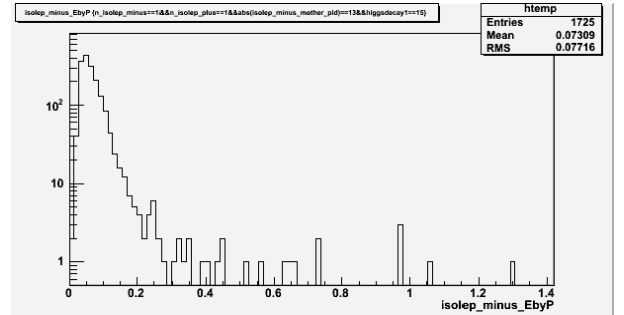
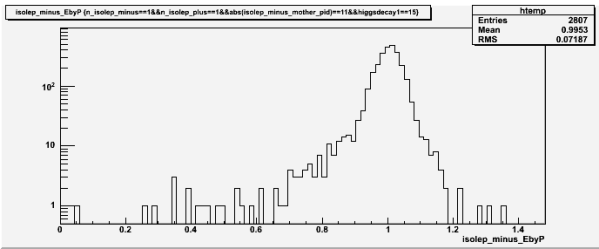


Figure 6: The plot of  $(E_{\text{ECAL}} + E_{\text{HCAL}})/P_{\text{track}}$  for the  $e$  in  $e^+e^-h$  samples.

Figure 7: The plot of  $(E_{\text{ECAL}} + E_{\text{HCAL}})/P_{\text{track}}$  for the  $\mu$  in  $\mu^+\mu^-h$  samples.

From these plots, we define the criteria for lepton identification. The criteria for electron identification ( $e$ -ID) and muon identification ( $\mu$ -ID) are summarized in Table 1.

After the lepton identification, we apply selections to remove secondary leptons from tau decays. The strategy of this selection is to remove tracks which do not come from the interaction point (IP) by using the track energy  $E_{\text{track}}$  and impact parameter in the transverse direction  $d_0$  and longitudinal direction  $z_0$  with respect to the beam axis. Figures 8 - 13 show the  $|d_0/\sigma(d_0)|$ ,  $|z_0/\sigma(z_0)|$ , and  $E_{\text{track}}$  plots which through the lepton identification.

Table 1: The criteria for lepton identification for  $Z \rightarrow \ell^+ \ell^-$  mode at  $\sqrt{s} = 250$  GeV.

	$e$ -ID	$\mu$ -ID
$E_{\text{ECAL}}/(E_{\text{ECAL}} + E_{\text{HCAL}})$	$> 0.92$	$< 0.6$
$(E_{\text{ECAL}} + E_{\text{HCAL}})/P_{\text{track}}$	$> 0.5$	$< 0.5$

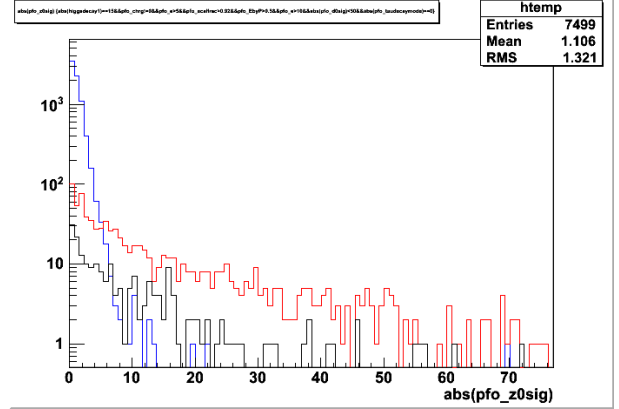
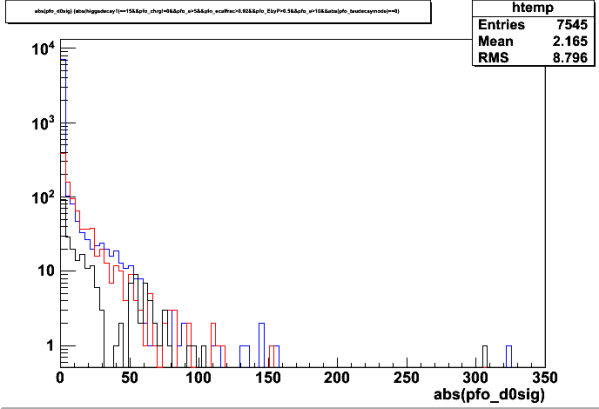


Figure 8: The plot of  $|d_0/\sigma(d_0)|$  of  $e$  of  $e^+e^-h$  process. Figure 9: The plot of  $|z_0/\sigma(z_0)|$  of  $e$  of  $e^+e^-h$  process. Blue, red, and black histograms show the  $e$  from  $Z \rightarrow e^+e^-$ , the  $e$  from  $\tau \rightarrow e\nu_\tau\nu_e$ , and the hadrons from  $\tau$  decay, respectively.

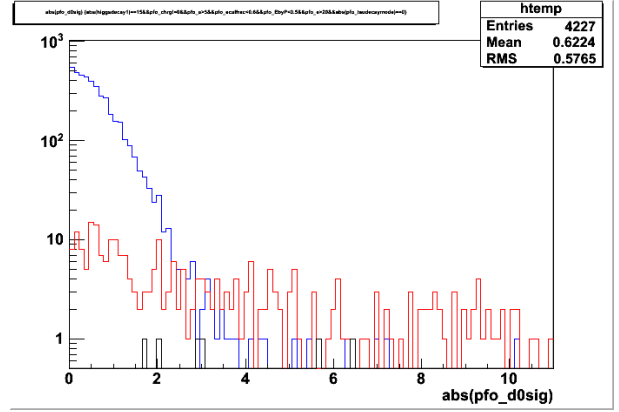
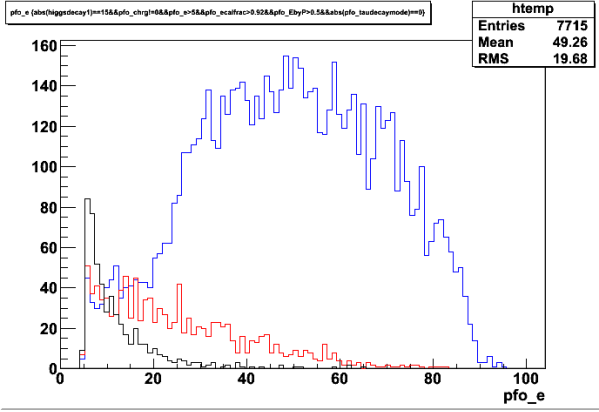


Figure 10: The plot of  $E_{\text{track}}$  of  $e$  of  $e^+e^-h$  process. Blue, red, and black histograms show the  $e$  from  $Z \rightarrow e^+e^-$ , the  $e$  from  $\tau \rightarrow e\nu_\tau\nu_e$ , and the hadrons from  $\tau$  decay, respectively. Figure 11: The plot of  $|d_0/\sigma(d_0)|$  of  $\mu$  of  $\mu^+\mu^-h$  process. Blue, red, and black histograms show the  $\mu$  from  $Z \rightarrow \mu^+\mu^-$ , the  $\mu$  from  $\tau \rightarrow \mu\nu_\tau\nu_\mu$ , and the hadrons from  $\tau$  decay, respectively.

We define the tau rejection cut for the objects through the  $e$ -ID and the  $\mu$ -ID respectively as shown in Table 2.

Table 2: The criteria for lepton identification for  $Z \rightarrow \ell^+ \ell^-$  mode at  $\sqrt{s} = 250$  GeV.

	$e$ -ID	$\mu$ -ID
$ d_0/\sigma(d_0) $	$< 50$	$< 3$
$ z_0/\sigma(z_0) $	$< 5$	$< 7$
$E_{\text{track}}$	$> 10$ GeV	$> 20$ GeV

We apply the energy recovery procedure to correct the effect of bremsstrahlung and final state radiation. In order to reconstruct the original  $Z$  boson, we have to use both the charged particles and the radiated photons. To achieve this, we define the cone as shown in Figure 14. The four-momenta of the neutral particles in the cone are combined with that of the lepton candidate. We define the half-opening angle of the cone with  $\cos\theta_{\text{cone}} = 0.999$  and apply the recovery procedure to the lepton candidates. The results are shown in Figures 15 and 16.

After that, we apply the tau finder to the remaining objects to reconstruct tau leptons. First of all, the objects which already used at  $Z$  boson reconstruction are rejected from tau reconstruction analysis. Then the finder searches the highest

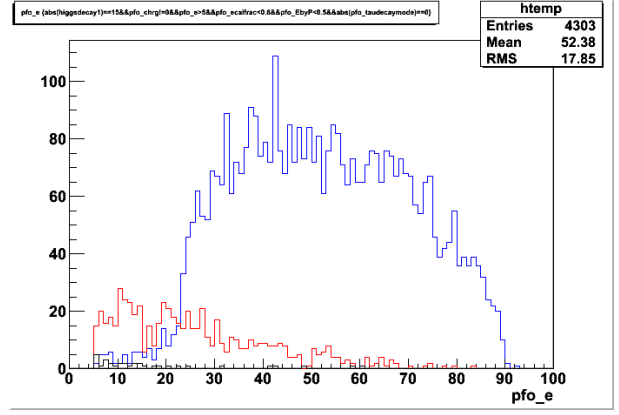
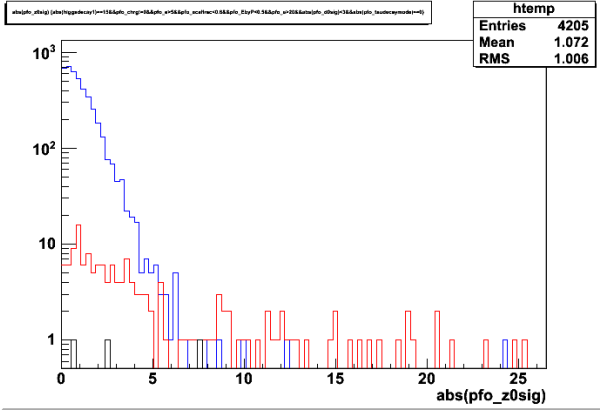


Figure 12: The plot of  $|z_0/\sigma(z_0)|$  of  $\mu$  of  $\mu^+\mu^-h$  process. Figure 13: The plot of  $E_{\text{track}}$  of  $\mu$  of  $\mu^+\mu^-h$  process. Blue, Blue, red, and black histograms show the  $\mu$  from  $Z \rightarrow \mu^+\mu^-$ ,  $\mu^+\mu^-$ , the  $\mu$  from  $\tau \rightarrow \mu\nu_\tau\nu_\mu$ , and the hadrons from  $\tau$  decay, respectively.

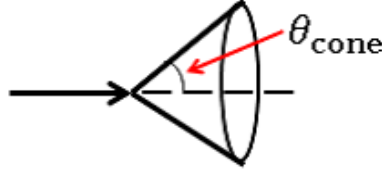


Figure 14: The definition of the cone. Black arrow shows the lepton candidate.  $\theta_{\text{cone}}$  is the angle of the cone.

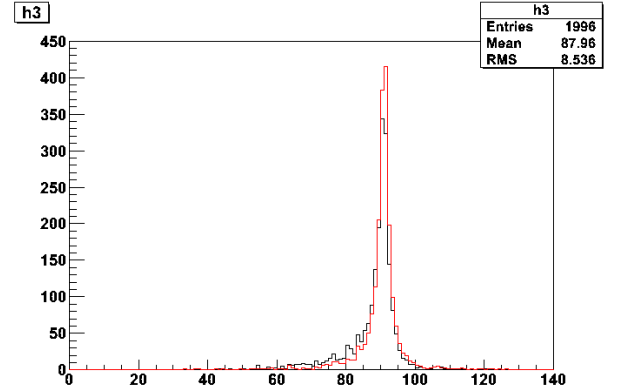
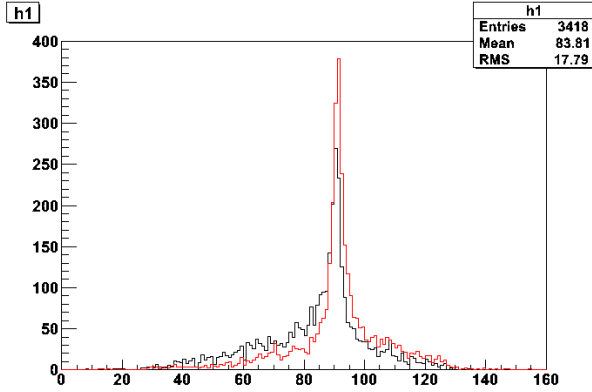


Figure 15: The results of recovery for  $Z \rightarrow e^+e^-$  mode. Figure 16: The results of recovery for  $Z \rightarrow \mu^+\mu^-$  mode. The horizontal axis shows the  $M_Z$ . Black and red histograms show the results of without recovery and with recovery ( $\cos \theta_{\text{cone}} = 0.999$ ), respectively.

energy track from the remaining objects, and combine the neighboring particles (which satisfies the angle with respect to the highest energy track less than 1.0 radian) with the combined mass less than 2 GeV. We regard the combined object as a tau candidate. Then repeat these processes until there are no charged particles.

After finishing the event reconstruction, we apply the cuts for selecting signal, rejecting background. Before optimizing the cuts, we apply the preselection as follows for  $Z \rightarrow e^+e^-$  mode: number of  $e^+$  and  $e^- = 1$ , number of  $\tau^+$  and  $\tau^- = 1$ , and for  $Z \rightarrow \mu^+\mu^-$  mode: number of  $\mu^+$  and  $\mu^- = 1$ , number of  $\tau^+$  and  $\tau^- = 1$ .

We apply the following cuts sequentially for  $Z \rightarrow e^+e^-$  mode: number of tracks  $\leq 8$ ,  $115 \text{ GeV} < E_{\text{vis}} < 230 \text{ GeV}$ ,  $|\cos \theta_{\text{miss}}| < 0.99$ ,  $81 \text{ GeV} < M_Z < 113 \text{ GeV}$ ,  $\cos \theta_{e^-} < 0.92$ ,  $\cos \theta_{e^+} > -0.92$ ,  $E_{e^-(e^+)} < 90 \text{ GeV}$ ,  $\cos \theta_{\tau^+\tau^-} < -0.45$ ,  $\cos \theta_{\tau^-} < 0.92$ ,  $\cos \theta_{\tau^+} > -0.92$ , and  $116 \text{ GeV} < M_{\text{recoil}} < 142 \text{ GeV}$ , where  $E_{\text{vis}}$  is the visible energy,  $\theta_{\text{miss}}$  is the missing momentum angle with respect to beam axis,  $\theta_{e^-(e^+)}$  is the  $e^-(e^+)$  angle with respect to beam axis,  $E_{e^-(e^+)}$  is the  $e^-(e^+)$  energy,  $\theta_{\tau^+\tau^-}$  is the angle between  $\tau^+$  and  $\tau^-$ ,  $\theta_{\tau^-(\tau^+)}$  is the  $\tau^-(\tau^+)$  angle with respect to beam axis, and  $M_{\text{recoil}}$  is the recoil mass, respectively. Figure 17 shows the recoil mass distribution. Table 3 shows the cut statistics of this mode. After the cuts, the  $Z \rightarrow e^+e^-$  signal events of 108.9 and background events of 76.0 remained. The statistical significance is calculated to be  $S/\sqrt{S+B} = 108.9/\sqrt{108.9+76.0} = 8.0\sigma$ .

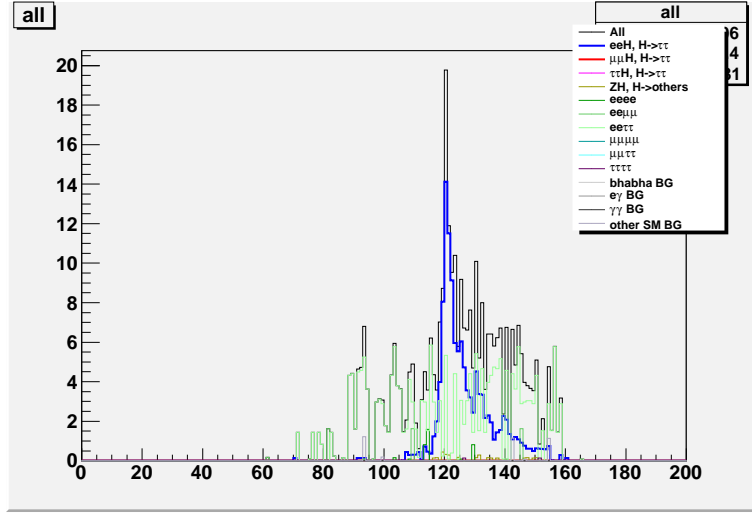


Figure 17: The distribution of recoil mass in the unit of GeV.

Table 3: The cut statistics of  $Z \rightarrow e^+e^-$  mode at  $\sqrt{s} = 250$  GeV.

	$e^+e^-h$ $h \rightarrow \tau^+\tau^-$	$\mu^+\mu^-h$ $h \rightarrow \tau^+\tau^-$	$\tau^+\tau^-h$ $h \rightarrow \tau^+\tau^-$	$Zh$ with $h \not\rightarrow \tau^+\tau^-$	$e^+e^-\tau^+\tau^-$	other 4 leptons	other SM bkg.	signi.
No cut	228.3	211.1	214.6	7325	$2.388 \times 10^5$	$5.238 \times 10^5$	$1.492 \times 10^{10}$	0.0019
preselection	171.3	0.155	1.532	47.05	$1.338 \times 10^4$	$3.215 \times 10^4$	$1.023 \times 10^7$	0.053
# of tracks	169.4	0.155	1.532	41.56	$1.316 \times 10^4$	$3.205 \times 10^4$	$1.009 \times 10^7$	0.053
$E_{\text{vis}}$	162.3	0.155	0.912	38.36	$1.068 \times 10^4$	$1.039 \times 10^4$	$4.761 \times 10^6$	0.074
$\cos \theta_{\text{miss}}$	160.6	0.155	0.912	38.03	8719	1906	$5.155 \times 10^5$	0.22
$M_Z$	148.0	0	0.017	29.09	2408	501.2	$1.299 \times 10^4$	1.2
$\cos \theta_{e^-(e^+)}$	133.9	0	0.009	25.40	1067	101.5	729.7	3.0
$E_{e^-(e^+)}$	133.0	0	0.009	24.93	690.3	78.70	629.7	3.4
$\cos \theta_{\tau^+\tau^-}$	130.8	0	0	3.536	254.9	30.70	155.4	5.5
$\cos \theta_{\tau^-(\tau^+)}$	123.4	0	0	3.074	212.1	9.161	3.817	6.6
$M_{\text{recoil}}$	108.9	0	0	2.474	72.35	1.134	0.034	8.0

We apply the following cuts sequentially for  $Z \rightarrow \mu^+\mu^-$  mode: number of tracks  $\leq 8$ ,  $115 \text{ GeV} < E_{\text{vis}} < 235 \text{ GeV}$ ,  $|\cos \theta_{\text{miss}}| < 0.98$ ,  $72 \text{ GeV} < M_Z < 107 \text{ GeV}$ ,  $E_{e^-(e^+)} < 90 \text{ GeV}$ ,  $\cos \theta_{\tau^+\tau^-} < -0.5$ , and  $118 \text{ GeV} < M_{\text{recoil}} < 143 \text{ GeV}$ . Figure 18 shows the recoil mass distribution. Table 4 shows the cut statistics of this mode. For the  $Z \rightarrow \mu^+\mu^-$  mode case, 131.2 signal events and 91.2 background events are remained. The significance is  $S/\sqrt{S+B} = 131.2/\sqrt{131.2+91.2} = 8.8\sigma$ .

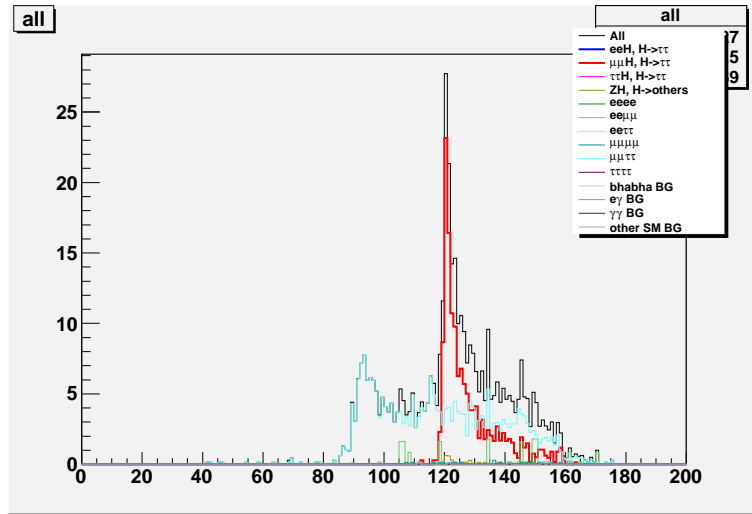


Figure 18: The distribution of recoil mass in the unit of GeV.

Table 4: The cut statistics of  $Z \rightarrow \mu^+\mu^-$  mode at  $\sqrt{s} = 250$  GeV.

	$\mu^+\mu^-h$ $h \rightarrow \tau^+\tau^-$	$e^+e^-h$ $h \rightarrow \tau^+\tau^-$	$\tau^+\tau^-h$ $h \rightarrow \tau^+\tau^-$	$Zh$ with $h \not\rightarrow \tau^+\tau^-$	$\mu^+\mu^-\tau^+\tau^-$	other 4 leptons	other SM bkg.	signi.
No cut	211.1	228.3	214.6	7325	3513	$7.591 \times 10^6$	$1.492 \times 10^{10}$	0.0017
preselection	168.5	0	0.155	43.01	1698	7546	7732	1.3
# of tracks	167.4	0	0.155	39.65	1684	7537	7400	1.3
$E_{\text{vis}}$	162.9	0	0.155	37.40	1586	2285	3713	1.9
$\cos\theta_{\text{miss}}$	158.6	0	0.155	36.51	1386	227.5	55.48	3.7
$M_Z$	153.2	0	0	32.84	1038	55.28	42.54	4.2
$E_{e^-(e^+)}$	153.2	0	0	32.70	738.6	42.41	36.72	4.8
$\cos\theta_{\tau^+\tau^-}$	146.3	0	0	3.638	259.4	20.19	0.756	7.1
$M_{\text{recoil}}$	131.2	0	0	2.875	82.36	5.311	0.301	8.8

## 4.2 $Z \rightarrow q\bar{q}$ mode at $\sqrt{s} = 250$ GeV

In this mode, the tau pairs are reconstructed first, followed by the dijet reconstruction of the  $Z$  decay.

At first we apply the tau finder to all objects to reconstruct taus. This tau finder searches the highest energy track and combine the neighboring particles, which satisfy  $\cos\theta_{\text{cone}} > 0.98$ , with the combined mass less than 2 GeV. We regard the combined object as a tau candidate. Then we apply the selection cuts as following:  $E_{\text{tau candidate}} > 3$  GeV,  $E_{\text{cone}} < 0.1E_{\text{tau candidate}}$  with  $\cos\theta_{\text{cone}} = 0.9$ , and rejecting 3-prong with neutral particles events. These selection cuts are tuned for minimizing misidentification of part of quark jets as tau jets. A survived tau candidate is regarded as a tau jet. After the selection cuts, we apply the charge recovery to obtain better efficiency. The charged particles in tau jet which have the energy less than 2 GeV are detached one by one from smallest energy from the tau jet until satisfying the conditions as following: the charge of tau jet is  $\pm 1$ , and the number of track(s) in tau jet is 1 or 3. The tau jet after detaching is rejected if it does not satisfy the above conditions. After the selection cuts and detaching, we repeat the above processes until there are no charged particles which have the energy greater than 2 GeV.

After the tau reconstruction, we apply the collinear approximation [15] to reconstruct tau pair. In this approximation, we assume that the visible decay products of tau and the neutrino(s) from tau is collinear, and the contribution of missing transverse momentum is only comes from the neutrino(s) of tau decay. The invariant mass of the tau pair with the collinear approximation shown in Figure 19.

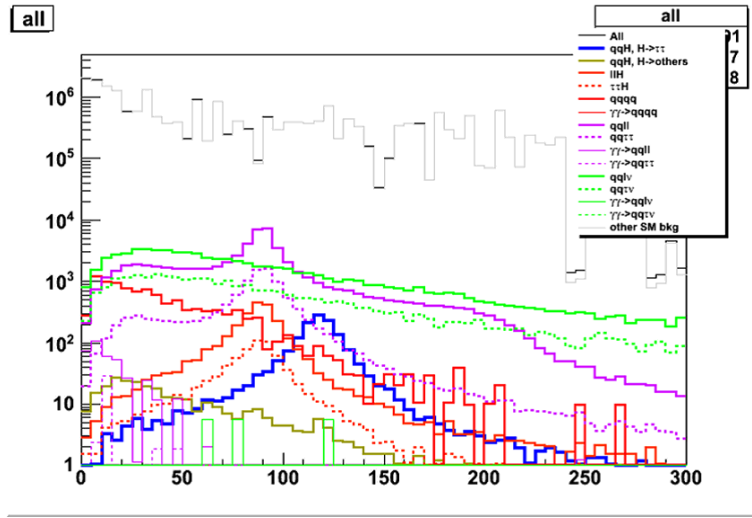


Figure 19: The plot of  $M_{\text{colapp}}$  in the unit of GeV, the invariant mass of tau pair with collinear approximation. Blue histogram shows the signal process  $Zh \rightarrow q\bar{q}\tau^+\tau^-$ .

After that, we apply the Durham jet clustering method [16] with two jets for the remaining objects to reconstruct  $Z$  boson.

After the all reconstruction, we apply the cuts to select signal process. Before optimizing cuts, we apply the preselection as follows: number of quark jets = 2, number of  $\tau^+$  and  $\tau^-$  = 1, number of tracks in a tau  $\leq 3$ , and the events which have tracks in both taus = 3 are rejected (double 3-prong cut). We apply the following cuts sequentially to reject the background:  $9 \leq \text{number of tracks} < 50$ ,  $110 \text{ GeV} < E_{\text{vis}} < 235 \text{ GeV}$ ,  $|\cos\theta_{\text{miss}}| < 0.98$ ,  $77 \text{ GeV} < M_Z < 135 \text{ GeV}$ ,  $80 \text{ GeV} < E_Z < 135 \text{ GeV}$ ,  $\cos\theta_{\tau^+\tau^-} < -0.5$ ,  $\log_{10}|d_0/\sigma(d_0)|(\tau^+) + \log_{10}|d_0/\sigma(d_0)|(\tau^-) > -0.7$ ,  $\log_{10}|z_0/\sigma(z_0)|(\tau^+) + \log_{10}|z_0/\sigma(z_0)|(\tau^-) > -0.1$ ,  $M_{\tau^+\tau^-} < 115 \text{ GeV}$ ,  $E_{\tau^+\tau^-} < 125 \text{ GeV}$ ,  $100 \text{ GeV} < M_{\text{colapp}} < 170 \text{ GeV}$ ,  $100 \text{ GeV} < E_{\text{colapp}} < 280 \text{ GeV}$ , and 112

GeV  $< M_{\text{recoil}} < 160$  GeV, where  $M_{\tau^+\tau^-}$  and  $E_{\tau^+\tau^-}$  is the invariant mass and energy of tau pair without using collinear approximation,  $M_{\text{colapp}}$  and  $E_{\text{colapp}}$  is the invariant mass and energy of tau pair with collinear approximation, respectively. Figure 20 shows the distribution of recoil mass. Table 5 shows the cut statistics of this mode. After the cuts, the signal events and background events are remained 1026 and 554.4. The statistical significance of  $Z \rightarrow q\bar{q}$  mode is calculated to be  $S/\sqrt{S+B} = 1026/\sqrt{1026+554.4} = 25.8\sigma$ .

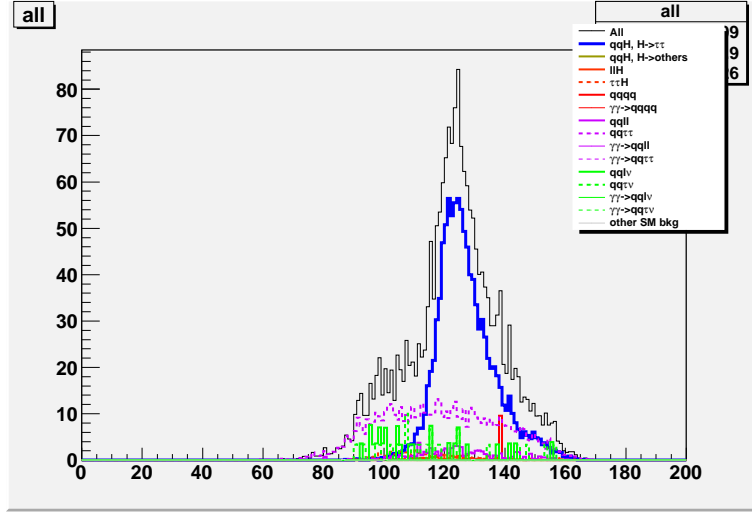


Figure 20: The distribution of recoil mass in the unit of GeV.

Table 5: The cut statistics of  $Z \rightarrow q\bar{q}$  mode at  $\sqrt{s} = 250$  GeV.

	$q\bar{q}h$ $h \rightarrow \tau^+\tau^-$	$Zh$ with $h \not\rightarrow \tau^+\tau^-$	$\ell^+\ell^-h$	$\tau^+\tau^-h$	$q\bar{q}q\bar{q}$	$q\bar{q}\ell^+\ell^-$	$q\bar{q}\tau^+\tau^-$	$q\bar{q}\ell\nu$	$q\bar{q}\tau\nu$	other SM bkg	signi.
No cut	4233	$4.829 \times 10^4$	5377	2596	$4.038 \times 10^6$	$3.563 \times 10^5$	$4.169 \times 10^4$	$2.788 \times 10^6$	$1.326 \times 10^6$	$1.494 \times 10^{10}$	0.035
preselection	1647	578.8	2761	765.4	$1.230 \times 10^4$	$6.378 \times 10^4$	$1.161 \times 10^4$	$1.249 \times 10^5$	$4.948 \times 10^4$	$2.570 \times 10^7$	0.32
# of tracks	1644	549.8	2680	765.4	$1.230 \times 10^4$	$6.059 \times 10^4$	$1.146 \times 10^4$	$1.214 \times 10^5$	$4.806 \times 10^4$	$5.190 \times 10^5$	1.9
$E_{\text{vis}}$	1607	492.3	1015	744.2	4443	$2.106 \times 10^4$	$1.107 \times 10^4$	$1.192 \times 10^5$	$4.693 \times 10^4$	$2.383 \times 10^5$	2.4
$\cos\theta_{\text{miss}}$	1572	474.7	860.5	725.1	2127	8315	$1.021 \times 10^4$	$1.171 \times 10^5$	$4.415 \times 10^4$	5939	3.6
$M_Z$	1440	376.1	791.3	682.8	778.6	4987	8674	8189	3288	997.3	8.3
$E_Z$	1429	352.0	782.7	528.7	505.0	4797	7857	7703	3061	609.9	8.6
$\cos\theta_{\tau^+\tau^-}$	1386	46.28	442.2	255.6	191.4	1468	2001	2831	1154	475.6	13.7
$d_0^{\text{sig}}$	1338	30.29	235.1	244.3	131.4	854.9	1928	1786	1044	248.1	15.1
$z_0^{\text{sig}}$	1287	19.54	105.0	234.7	81.77	408.2	1845	909.9	883.4	244.6	16.6
$M_{\tau^+\tau^-}$	1286	19.39	103.2	234.7	72.05	349.1	1837	883.5	883.4	243.9	16.7
$E_{\tau^+\tau^-}$	1282	19.39	103.0	234.7	72.05	324.7	1836	873.2	883.4	243.9	16.7
$M_{\text{colapp}}$	1065	3.074	18.76	47.94	10.28	72.83	616.9	150.8	137.0	0.746	23.1
$E_{\text{colapp}}$	1062	2.454	18.01	46.72	10.28	71.27	612.1	93.05	93.52	0.454	23.7
$M_{\text{recoil}}$	1026	2.144	14.54	21.24	9.938	57.07	366.3	39.64	43.31	0.161	25.8

### 4.3 $Z \rightarrow q\bar{q}$ mode at $\sqrt{s} = 500$ GeV

We take the same analysis strategy which described in Section 4.2. We apply the same tau finder to all objects to reconstruct taus from Higgs boson, followed by collinear approximation [15], then apply Durham algorithm [16] to remaining objects to reconstruct  $Z$  boson. Figure 21 shows the distribution of tau pair mass with collinear approximation for the signal process.

After the reconstruction we apply the cuts to select signal process. Before optimizing, we apply the preselection cut as; number of quark jet = 2, number of  $\tau^+(\tau^-) = 1$ , number of tracks in a tau  $\leq 3$ . Then we apply following cuts: number of tracks  $\geq 14$ , thrust  $< 0.93$ ,  $|\cos\theta_{\text{miss}}| < 0.95$ ,  $70 \text{ GeV} < M_Z < 265 \text{ GeV}$ ,  $E_Z > 135 \text{ GeV}$ ,  $20 \text{ GeV} < M_{\tau^+\tau^-} < 120 \text{ GeV}$ ,  $E_{\tau^+\tau^-} < 235 \text{ GeV}$ ,  $\cos\theta_{\tau^+\tau^-} < 0.56$ ,  $115 \text{ GeV} < M_{\text{colapp}} < 135 \text{ GeV}$ ,  $205 \text{ GeV} < E_{\text{colapp}} < 270 \text{ GeV}$ ,  $\log_{10}|d_0/\sigma(d_0)|(\tau^+) + \log_{10}|d_0/\sigma(d_0)|(\tau^-) > 0.4$ , and  $\log_{10}|z_0/\sigma(z_0)|(\tau^+) + \log_{10}|z_0/\sigma(z_0)|(\tau^-) > -0.1$ . Figure 22 shows the distribution of  $\log_{10}|z_0/\sigma(z_0)|(\tau^+) + \log_{10}|z_0/\sigma(z_0)|(\tau^-)$ . Table 6 shows the cut statistics of this mode. The statistical significance of this mode is calculated to be  $S/\sqrt{S+B} = 453.7/\sqrt{453.7+219.5} = 17.5\sigma$ . This result corresponds to the precision of  $\Delta(\sigma \cdot \text{Br})/(\sigma \cdot \text{Br}) = 5.7\%$

### 4.4 $WW$ -fusion process at $\sqrt{s} = 500$ GeV

At first in this mode, we apply the  $k_T$  algorithm [17,18] to remove objects from  $\gamma\gamma \rightarrow \text{hadron(s)}$  overlaid process. We use **FastJet** package [19] as the  $k_T$  clustering package. We choose the value of generalized radius  $R$  of  $k_T$  clustering of 1.0 currently (more optimization needed).



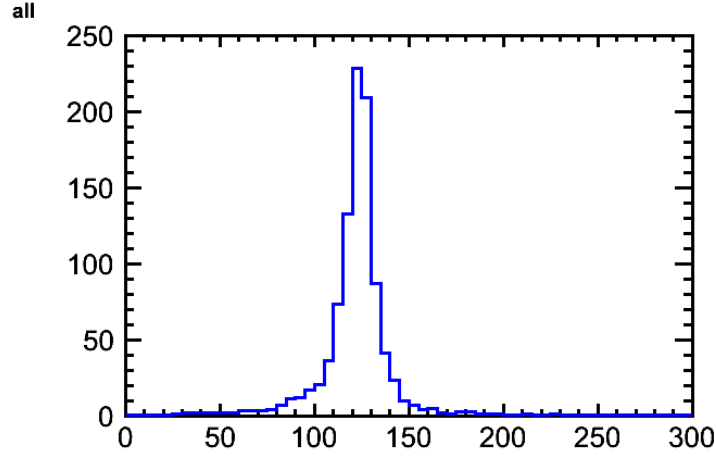


Figure 21: The plot of  $M_{\text{colapp}}$  of the signal process  $Zh \rightarrow q\bar{q}\tau^+\tau^-$  in the unit of GeV, the invariant mass of tau pair with collinear approximation.

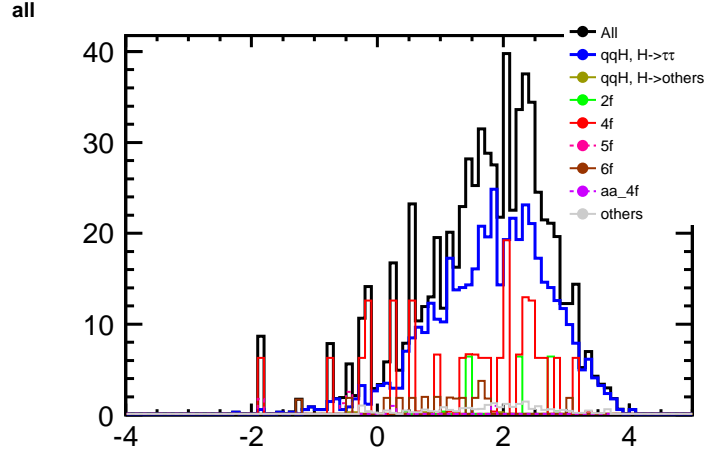


Figure 22: The distribution of  $\log_{10} |z_0/\sigma(z_0)|(\tau^+) + \log_{10} |z_0/\sigma(z_0)|(\tau^-)$ .

Table 6: The cut statistics of  $Z \rightarrow q\bar{q}$  mode at  $\sqrt{s} = 500$  GeV.

	$q\bar{q}h$ $h \rightarrow \tau^+\tau^-$	$q\bar{q}h$ with $h \not\rightarrow \tau^+\tau^-$	2f	4f	5f	6f	$\gamma\gamma \rightarrow 4f$	$\ell^+\ell^-h, \nu\bar{\nu}h$	signi.
No cut	2158	$3.139 \times 10^4$	$1.320 \times 10^7$	$1.598 \times 10^7$	$6.895 \times 10^4$	$5.887 \times 10^5$	$1.041 \times 10^5$	$9.510 \times 10^4$	0.39
preselection	1019	604.9	$1.151 \times 10^6$	$1.125 \times 10^6$	9713	$4.001 \times 10^4$	$1.349 \times 10^4$	7694	0.67
# of tracks	994.5	600.8	$1.569 \times 10^5$	$3.498 \times 10^5$	6960	$3.879 \times 10^4$	5187	5403	1.3
thrust	964.1	574.5	$7.176 \times 10^4$	$1.821 \times 10^5$	6663	$3.852 \times 10^4$	4822	5821	1.7
$\cos \theta_{\text{miss}}$	898.3	486.4	$1.741 \times 10^4$	$1.174 \times 10^5$	4195	$3.508 \times 10^4$	2379	3955	2.1
$M_Z$	855.3	321.2	7682	$7.962 \times 10^4$	3467	$2.488 \times 10^4$	1741	3441	2.5
$E_Z$	849.7	318.5	5164	$6.666 \times 10^4$	2884	$2.282 \times 10^4$	1243	3147	2.7
$M_{\tau^+\tau^-}$	806.1	259.4	1530	$4.243 \times 10^4$	1483	$1.687 \times 10^4$	665.4	1974	3.1
$E_{\tau^+\tau^-}$	800.3	258.0	1154	$3.465 \times 10^4$	1436	$1.684 \times 10^4$	645.7	1112	3.4
$\cos \theta_{\tau^+\tau^-}$	795.9	137.5	744.6	$2.699 \times 10^4$	1093	$1.471 \times 10^4$	490.4	472.8	3.7
$M_{\text{colapp}}$	557.8	6.435	52.91	770.4	38.19	579.6	17.78	36.81	12.3
$E_{\text{colapp}}$	511.3	5.265	38.91	351.5	20.44	90.13	7.943	31.67	15.7
$d_0\text{sig}$	468.6	2.047	20.44	179.9	5.623	28.35	1.995	24.30	17.3
$z_0\text{sig}$	453.7	1.462	20.44	148.4	0	24.57	1.995	22.58	17.5

We apply the same tau finder which described in Section 4.1 to all survived objects through the  $k_T$  clustering, the only difference is the maximum associated angle has been changed from 1.0 radian to 0.76 radian. The most energetic  $\tau^+$  candidate and  $\tau^-$  candidate are combined as it comes from Higgs boson.

After the reconstruction, we apply the preselection as the number of  $\tau^+(\tau^-) \geq 1$ , because the  $\gamma\gamma \rightarrow \text{hadron(s)}$  processes produce additional charged particles, and the tau finder which used for this process repeat finding process until there are no charged particles.

Then we apply following cuts: number of tracks  $\leq 6$ ,  $5 \text{ GeV} < M_{\text{vis}} < 135 \text{ GeV}$ ,  $E_{\text{vis}} < 240 \text{ GeV}$ ,  $P_t > 25 \text{ GeV}$ ,  $|\cos \theta_{\text{miss}}| < 0.89$ ,  $M_{\tau^+\tau^-} < 115 \text{ GeV}$ ,  $-0.86 < \cos \theta_{\tau^+\tau^-} < 0.57$ ,  $\cos \theta_{\text{acop}} < 0.99$ ,  $\log_{10} |\min(d_0/\sigma(d_0))| > 0.3$ ,  $\log_{10} |\min(z_0/\sigma(z_0))| > 0$ , where  $M_{\text{vis}}$  is visible energy,  $\theta_{\text{acop}}$  is acoplanarity,  $\min(d_0/\sigma(d_0))$  ( $\min(z_0/\sigma(z_0))$ ) is smaller impact parameter value between  $\tau^+$  and  $\tau^-$ , respectively. Figure 23 shows the distribution of  $\log_{10}(\min(z_0/\sigma(z_0)))$ . Table 7 shows the cut statistics of this mode. The statistical significance of this mode is calculated to be  $S/\sqrt{S+B} = 1469/\sqrt{1469+1.061 \times 10^4} = 13.4\sigma$ .

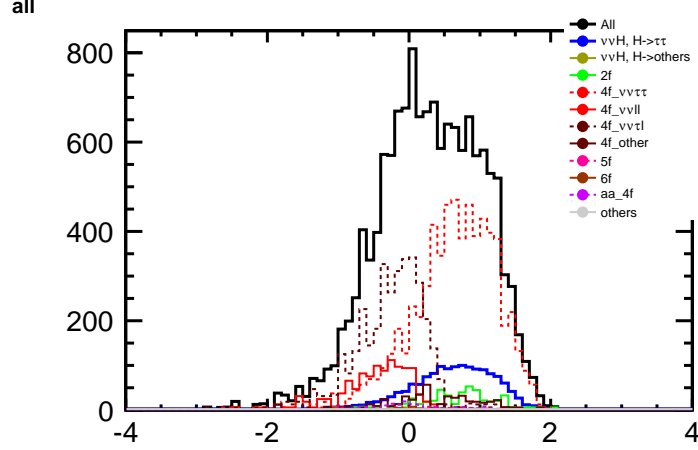


Figure 23: The distribution of  $(\min(z_0/\sigma(z_0)))$ .

Table 7: The cut statistics of  $WW$ -fusion process at  $\sqrt{s} = 500 \text{ GeV}$ .

	$\nu\bar{\nu}h$ $h \rightarrow \tau^+\tau^-$	$\nu\bar{\nu}h$ with $h \not\rightarrow \tau^+\tau^-$	2f	4f $\nu\bar{\nu}\tau^+\tau^-$	4f others	5f	6f	$\gamma\gamma \rightarrow 4f$	$\ell^+\ell^-h, q\bar{q}h$	signi.
No cut	5401	$7.967 \times 10^4$	$1.335 \times 10^7$	$1.452 \times 10^7$	$1.594 \times 10^7$	$6.895 \times 10^4$	$5.895 \times 10^5$	$1.041 \times 10^5$	$4.363 \times 10^4$	0.98
preselection	4676	6062	$3.973 \times 10^6$	$1.070 \times 10^5$	$4.215 \times 10^6$	$2.093 \times 10^4$	$2.344 \times 10^4$	$4.132 \times 10^4$	2650	1.6
# of tracks	4274	2461	$2.649 \times 10^6$	$9.896 \times 10^4$	$2.457 \times 10^6$	$1.123 \times 10^4$	7035	$2.782 \times 10^4$	1126	1.9
$M_{\text{vis}}$	4258	2394	$8.030 \times 10^5$	$5.527 \times 10^4$	$1.087 \times 10^6$	7220	2773	$2.458 \times 10^4$	262.9	3.0
$E_{\text{vis}}$	4251	2386	$5.846 \times 10^5$	$5.511 \times 10^4$	$9.096 \times 10^5$	6886	2736	$2.357 \times 10^4$	205.9	3.4
$P_t$	3992	2166	$4.232 \times 10^5$	$4.580 \times 10^4$	$5.043 \times 10^5$	5229	2683	9244	205.9	4.0
$\cos \theta_{\text{miss}}$	3294	1876	$6.745 \times 10^4$	$3.051 \times 10^4$	$1.967 \times 10^5$	2702	1978	4368	148.7	5.9
$M_{\tau^+\tau^-}$	3245	1865	$5.612 \times 10^4$	$2.653 \times 10^4$	$1.759 \times 10^5$	2485	1696	4157	141.7	6.2
$\cos \theta_{\tau^+\tau^-}$	2837	923.6	$1.495 \times 10^4$	$1.416 \times 10^4$	$1.085 \times 10^5$	1757	1224	2866	64.59	7.4
$\cos \theta_{\text{acop}}$	2742	909.3	7384	$1.367 \times 10^4$	$1.050 \times 10^5$	1722	1201	2792	63.65	7.5
$d_0\text{sig}$	1733	77.50	745.2	8293	8051	159.9	134.0	261.7	11.71	12.4
$z_0\text{sig}$	1469	40.49	542.5	6989	2744	84.90	76.22	126.4	7.755	13.4

In  $\nu\bar{\nu}h$  events, there are two contributions from  $WW$ -fusion and Higgs-strahlung. The number of remained events can be written as:

$$N_{\text{remained}} = L \left( \sum_{i=e,\mu,\tau} \sigma_{Zh} \times \text{Br}(Z \rightarrow \nu_i \bar{\nu}_i) \times \text{Br}(h \rightarrow \tau^+\tau^-) \times \varepsilon_1 + \sigma_{WW\text{-fusion}} \times \text{Br}(h \rightarrow \tau^+\tau^-) \times \varepsilon_2 \right),$$

where  $\varepsilon_1$  and  $\varepsilon_2$  are the selection efficiency for Higgs-strahlung process and  $WW$ -fusion process, respectively. The signal significance is for the  $\sum_{i=e,\mu,\tau} \sigma_{Zh} \times \text{Br}(Z \rightarrow \nu_i \bar{\nu}_i) \times \text{Br}(h \rightarrow \tau^+\tau^-) + \sigma_{WW\text{-fusion}} \times \text{Br}(h \rightarrow \tau^+\tau^-)$ .

## 5 Summary and Prospects

We evaluate the measurement accuracy of the branching ratio of the  $h \rightarrow \tau^+\tau^-$  mode at  $\sqrt{s} = 250 \text{ GeV}$  and  $500 \text{ GeV}$  at the ILC with ILD detector full simulation. For the analysis of  $\sqrt{s} = 250 \text{ GeV}$ , we assume  $M_h = 120 \text{ GeV}$ ,  $\text{Br}(h \rightarrow \tau^+\tau^-) = 8.0 \%$ ,  $\int L dt = 250 \text{ fb}^{-1}$ , and beam polarization  $P(e^+, e^-) = (+0.3, -0.8)$ . The analysis results and scaled results to  $M_h = 125 \text{ GeV}$  are summarized in Table 8.

For the  $\sqrt{s} = 500 \text{ GeV}$ , the analyses are still ongoing, but we obtain the statistical significance and measurement accuracy as summarized in Table 9, with assuming  $M_h = 125 \text{ GeV}$ ,  $\text{Br}(h \rightarrow \tau^+\tau^-) = 6.32 \%$ ,  $\int L dt = 500 \text{ fb}^{-1}$ , and beam polarization  $P(e^+, e^-) = (+0.3, -0.8)$ . The result of  $WW$ -fusion is better than the expected accuracy in the Technical Design Report [12]. We expect improvement by better treatment of  $\gamma\gamma \rightarrow \text{hadron(s)}$  background and more optimizing tau reconstruction.

Table 8: The analysis results of  $\sqrt{s} = 250$  GeV with assuming  $M_h = 120$  GeV and scaled results to  $M_h = 125$  GeV.

	$Z \rightarrow e^+e^-$	$Z \rightarrow \mu^+\mu^-$	$Z \rightarrow q\bar{q}$	Combined	$\frac{\Delta(\sigma \cdot \text{Br})}{(\sigma \cdot \text{Br})}$
Results of $M_h = 120$ GeV	$8.0\sigma$	$8.8\sigma$	$25.8\sigma$	$28.4\sigma$	3.5 %
Scaled results to $M_h = 125$ GeV	$6.8\sigma$	$7.4\sigma$	$21.9\sigma$	$24.1\sigma$	4.2 %

Table 9: The analysis results of  $\sqrt{s} = 500$  GeV with assuming  $M_h = 125$  GeV.

	$Z \rightarrow q\bar{q}$	$WW$ -fusion
significance	$17.5\sigma$	$13.4\sigma$
$\frac{\Delta(\sigma \cdot \text{Br})}{(\sigma \cdot \text{Br})}$	5.7 %	7.5 %

## References

- [1] G.Aad *et al.* [ATLAS Collaboration], Phys. Lett. B **716** (2012) 1 - 29
- [2] S. Chatrchyan *et al.* [CMS Collaboration], Phys. Lett. B **716** (2012) 30 - 61
- [3] R. S. Gupta, H. Rzehak, J. D. Wells, Phys. Rev. D **86**, 095001 (2012)
- [4] P. Mora de Fretias, H. Videau, LC-TOOL-2003-010 (2003)
- [5] S. Agostinelli *et al.* [GEANT4 Collaboration], Nucl. Instrum. Meth. A **506**, 250 - 303 (2003).
- [6] S. Jadach, J. H. Kühn, Z. Was, Comput. Phys. Commun. **64** (1991) 275 - 299
- [7] ILD Concept Group, "The International Large Detector — Letter of Intent" (2010)
- [8] <http://ilcsoft.desy.de/portal>
- [9] T. Sjöstrand, S. Mrenna, P. Skands, JHEP 0605, 026 (2006)
- [10] S. Dittmaier, C. Mariotti, G. Passarino, R. Tanaka, *et al.* [LHC Higgs Cross Section Working Group], arXiv:1201.3084v1 [hep-ph] (2012)
- [11] The International Linear Collider Technical Design Report Volume 1: Executive Summary (2013)
- [12] The International Linear Collider Technical Design Report Volume 2: Physics (2013)
- [13] The International Linear Collider Technical Design Report Volume 3: Accelerator (2013)
- [14] The International Linear Collider Technical Design Report Volume 4: Detectors (2013)
- [15] R. K. Ellis, I. Hinchliffe, M. Soldate, J. J. van der bij, Nucl. Phys. B **297** (1988) 221 - 243
- [16] S. Catani, Y. L. Dokshitzer, M. Olsson, G. Turnock, B. R. Webber, Phys. Lett. B **269** (1991) 432 - 438
- [17] S. Catani, Y. L. Dokshitzer, M. H. Seymour, B. R. Webber, Nucl. Phys. B **406** (1993) 187 - 224
- [18] S. D. Ellis, D. E. Soper, Phys. Rev. D. **48**, 7 (1993)
- [19] M. Cacciari, G. P. Salam, G. Soyez, arXiv:1111.6097v1 [hep-ph] (2011)